



HAL
open science

Influence of recent climatic events on the surface water storage of the Tonle Sap Lake

Frédéric Frappart, Sylvain Biancamaria, C. Normandin, F. Blarel, L. Bourrel, M. Aumont, P. Azemar, P. L. Vu, Thuy Le Toan, B. Lubac, et al.

► **To cite this version:**

Frédéric Frappart, Sylvain Biancamaria, C. Normandin, F. Blarel, L. Bourrel, et al.. Influence of recent climatic events on the surface water storage of the Tonle Sap Lake. *Science of the Total Environment*, 2018, 636, pp.1520-1533. 10.1016/j.scitotenv.2018.04.326 . hal-02272424

HAL Id: hal-02272424

<https://hal.science/hal-02272424v1>

Submitted on 27 Aug 2019

HAL is a multi-disciplinary open access archive for the deposit and dissemination of scientific research documents, whether they are published or not. The documents may come from teaching and research institutions in France or abroad, or from public or private research centers.

L'archive ouverte pluridisciplinaire **HAL**, est destinée au dépôt et à la diffusion de documents scientifiques de niveau recherche, publiés ou non, émanant des établissements d'enseignement et de recherche français ou étrangers, des laboratoires publics ou privés.

1 **Influence of recent climatic events on the surface water storage of the Tonle Sap Lake**

2

3 Frappart F. (1,2), Biancamaria S. (2), Normandin C. (3), Blarel F. (2), Bourrel L. (1), Aumont

4 M. (2), Azemar P. (2), Vu P-L. (1), T. Le Toan (4), Lubac B. (3), Darrozes J. (1)

5

6 (1) Géosciences Environnement Toulouse (GET), UMR 5563, CNRS/IRD/Université de

7 Toulouse, OMP-GRGS, 14 Avenue Edouard Belin, 31400 Toulouse, France

8 (2) LEGOS, Université de Toulouse, CNES, CNRS, IRD, UPS - 14 avenue Edouard Belin,

9 31400 Toulouse, France

10 (3) Environnement et Paléo-Environnement Océaniques et Continentaux (EPOC), UMR

11 5805, CNRS/Université de Bordeaux, Allée Geoffroy Saint-Hilaire, 33615 Pessac, France

12 (4) Centre d'Etudes Spatiales de la Biosphère (CESBIO), UMR 5126,

13 CNRS/CNES/IRD/Université de Toulouse, 13 Avenue du Colonel Roche, 31400 Toulouse,

14 France

15

16 Published in *Science of the Total Environment*, <https://doi.org/10.1016/j.scitotenv.2018.04.326>

17

18

19 **Abstract:**

20
21 Lakes and reservoirs have been identified as sentinels of climate change. Tonle Sap is the
22 largest lake in both the Mekong Basin and Southeast Asia and because of the importance of
23 its ecosystem, it is has been described as the “heart of the lower Mekong”. Its seasonal cycle
24 depends on the annual flood pulse governed by the flow of the Mekong River. This study
25 provides an impact analysis of recent climatic events from El Niño 1997/1998 to El
26 Niño 2015/2016 on surface storage variations in the Tonle Sap watershed determined by
27 combining remotely sensed observations, multispectral images and radar altimetry from 1993
28 to 2017. The Lake’s surface water volume variations are highly correlated with rainy
29 season rainfall in the whole Mekong River Basin ($R=0.84$) at interannual time-scale.
30 Extreme droughts and floods can be observed when precipitation deficit and excess is
31 recorded in both the Tonle Sap watershed and the Mekong River Basin during moderate to
32 very strong El Niño/La Niña events ($R=-0.70$) enhanced by the Pacific Decadal Oscillation
33 ($R=-0.68$). Indian and Western North Pacific Monsoons were identified as having almost
34 equal influence. Below normal vegetation activity was observed during the first semester of
35 2016 due to the extreme drought in 2015.

36
37 Keywords : Surface water storage; Rainfall; ENSO; PDO; Monsoon; E VI; Mekong
38 Basin; Multi-satellite

1. Introduction

Climate variability and human population growth have led to inland waters being identified as some of the most severely endangered ecosystems (Rosenzweig et al., 2007). Lakes and reservoirs are widely distributed around the world and act as integrators of changes occurring in their watershed, the surrounding landscape and the atmosphere (Schindler, 2009; Williamson et al., 2009a). As their physical, chemical, and biological properties respond rapidly to climate-induced changes, they offer a valuable source of information for assessing and monitoring the effects of climate change (e.g., Magnuson, 2000; Lemoalle et al., 2012). Lakes and reservoirs are commonly seen as sentinels of climate change as their physical, chemical, and biological responses to climate variations integrate the changes occurring in their catchment (Adrian et al., 2009; Schindler, 2009; C. E. Williamson et al., 2009).

Tonle Sap Lake in Cambodia is the largest lake and wetland ecosystem in the Mekong River Basin (MRC, 2005). It is considered as the “heart of the Lower Mekong” due to the exceptional biodiversity of its ecosystem (Campbell et al., 2006) and is also one of the most productive ecosystems in the world (Lamberts, 2006) with its high productivity being linked to the flood pulse of the Mekong River (Kummu et al., 2006). The hydrological cycle in the Mekong River Basin is governed by the monsoon regime, itself being strongly influenced by El Niño Southern Oscillation (ENSO). El Niño events are responsible for a decrease in the rainfall, discharge and annual flood period (Räsänen and Kummu, 2013). Conversely, La Niña increases the rainfall, discharge and annual flood period. The combination of climate-related and anthropogenic (hydropower, irrigation) changes in the Mekong River Basin are expected to cause large modifications to the flood pulse of the Tonle Sap (Kummu and Sarkkula, 2008; Västilä et al., 2010). The frequency and intensity of drought and flood events in the region have increased over the past few decades, impacting irrigated fields (Cruz et al.,

2007; Kamoshita and Ouk, 2015). Dam construction and operations in the Chinese Upper Mekong Basin are also altering the hydrological regime in the Lower Mekong Basin (Stone, 2010; Lu et al., 2014). Development of new hydropower dams in the Chinese Upper Mekong Basin combined with possible development of thirty-eight new dams in the Vietnamese Lower Mekong Basin will have a major impact on the hydrological regime of this region (see Lu et al., 2014 for the impacts on the Chinese Upper Mekong Basin; Arias et al., 2014 for the impacts on the Vietnamese Lower Mekong Basin).

Remotely sensed observations offer a unique opportunity to continuously monitor floods in large watersheds. Previous studies have determined spatio-temporal flooding extent by applying a threshold approach to land surface reflectances, or spectral indexes from the MODerate resolution Imaging Sensor (MODIS) radiometer (Sakamoto et al., 2007; Arias et al., 2012; Siev et al., 2016; Fayne et al., 2017) in the Tonle Sap watershed. Gravity Recovery and Climate Experiment (GRACE) products have recently been used along with MODIS images to estimate total water storage and identify flood events in the Tonle Sap watershed (Tangdamrongsub et al., 2016). Estimates of surface water volume changes in the Tonle Sap watershed are sparse and have only been for short time-periods (e.g., 1997-2005 in Kummu and Sarkkula, 2008; and 2003-2005 in Siev et al., 2016).

The purpose of this study is to estimate Tonle Sap lake storage variations over the two last decades and analyze the link between its annual variations with atmospheric forcing, especially climatic oscillations. Surface water storage variations of the lake are computed over the 1993-2017 time span, through a synergistic use of flood extent derived from MODIS land surface reflectances (see sections 3.1 and 4.1) and altimetry-based water levels (see sections 3.2 and 4.2). During these two decades, three extreme droughts (1998, 2015, and 2016) and three exceptional floods (2000, 2002, and 2011) occurred in the Tonle Sap watershed. In the following, relationships with climate variability are discussed through comparisons with climate indices (sections 3.3 and 5.2). A first impact assessment of the extreme drought of

2015 on the Tonle Sap ecosystem is also presented.

2. Study area

Ninety-five percent of the Tonle Sap Lake drainage area is located in Cambodia, with the remaining five percent in Thailand. It is the largest lake and wetland in the Mekong River Basin and the largest lake in Southeast Asia (MRC, 2005; Campbell et al., 2009). Its whole drainage basin occupies an area of 85,800 km² (i.e., 11% of the whole surface of the Mekong basin, MRC 2003) (Fig. 1). The lake-floodplain system extends from 2,400 km² during the low water period to 16,000 km² at peak flood during wet years (Lim et al., 1999; Kummur and Sarkkula, 2008).

The catchment incorporates five different land cover classes, as described by Arias et al., (2012):

- Open water (under water from 9 to 12 months a year and covering an area of 3,027 km²),
- Gallery forest (annually flooded for 9 months and covering an area of 197 km²)
- Seasonally flooded habitats, composed of shrublands and grasslands (annually flooded from 5 to 8 months on average and covering an area of 5,409 km²)
- Transitional habitats dominated by abandoned agricultural fields, receding rice/floating rice, and lowland grasslands (annually flooded from 1 to 5 months on average and covering an area of 3,658 km²)
- Rainfed habitats mostly composed of wet season rice fields and village crops (flooded less than 1 month per year and covering an area of 8,641 km²)

Tonle Sap Lake is an important ecosystem of Southeast Asia due to its exceptional biodiversity (Campbell et al., 2006). It has been internationally recognized through three Biosphere Reserve core areas under the United Nations Educational, Scientific and Cultural Organization (UNESCO) Programme on Man and the Biosphere (UNESCO, 2006), as well as one Ramsar site under the Ramsar Convention on wetlands (see www.ramsar.org). The Tonle

116 Sap lake ecosystem also supports important fisheries and aquaculture activities. These
117 industries sustain over one million people (Rainboth, 1996; Sverdrup-Jensen, 2002; Horte,
118 2007).

119 The annual monomodal flood pulse in Tonle Sap Lake is governed by the flow in the Mekong
120 River (Junk et al., 2006; Lamberts, 2006). The Tonle Sap River connects the lake to the
121 Mekong River. In the May to September wet season its flow direction is inversed due to water
122 level increase in the Mekong River (Kummu and Sarkkula, 2008). Annual average inflow and
123 outflow are 79.0 and 78.6 km³, respectively. 57% of the inflow comes from the Mekong
124 mainstem, either through Tonle Sap River discharge (52%) or by overland flooding (5%)
125 (MRCS/WUP-FIN, 2006).

126 The contributions of Tonle Sap Lake tributaries and direct rainfall into the lake are estimated
127 at around 30% and 13%, respectively (Kummu et al., 2014). Water receding from the lake
128 mostly flows into the Mekong River (88%) or evaporates (12%) (Kummu et al., 2014).

129

130 **3. Datasets**

131 3.1. Surface reflectances from MODIS

132 The MODIS spectroradiometer is part of the payload of the Aqua and Terra satellites (launched in
133 2002 and 1999, respectively). The MODIS sensor acquires radiances in 36 spectral bands. In this
134 study, the MOD09A1 product (8-day binned level 3, version 6) derived from Terra raw radiance
135 measurements were downloaded from the United States Geological Survey (USGS) Earthexplorer
136 website (<http://earthexplorer.usgs.gov>). It consists in gridded surface reflectances acquired in 7 bands
137 from 620 nm (Red) to 2155 nm (SWIR2) at a resolution of 500 m and corrected for atmospheric
138 effect. This product is obtained by combining the best surface reflectance data of every pixel acquired
139 during an 8-day period for each wavelength. Each MODIS tile covers an area of 1200 km by 1200 km.
140 In this study, 815 composite images from February 2000 to December 2017 were used.

141
142
143
144
145
146
147
148
149
150
151
152
153
154
155
156
157
158
159
160
161
162
163
164
165
166

3.2. Radar altimetry data

Our radar altimetry data comes from the acquisitions on their nominal orbit of the following missions: Topex-Poseidon (1992-2002), Jason-1 (2002-2008), Jason-2 (2008-2016), Jason-3 (since 2016), ERS-2 (1995-2003), ENVISAT (2003-2010), and SARAL (2013-2016). Topex/Poseidon and Jason-1 to -3 missions are on the same 10-day repeat period orbit, whereas ERS-2, ENVISAT and SARAL succeed each other on the same 35-day repeat-period orbit. Altimetry data comes from Geophysical Data Records (GDR) E for Jason-1; GDR D for Jason-2, Jason-3 and SARAL; and GDR v2.1 for ENVISAT delivered by CNES/ESA/NASA processing centers. The data was homogenized and made available by Centre de Topographie des Océans et de l’Hydrosphère (CTOH – <http://ctoh.legos.obs-mip.fr>). ERS-2 data was reprocessed by CTOH to ensure continuity with ENVISAT for land studies (Frappart et al., 2016). Topex/Poseidon time series come from Frappart et al., (2006b).

3.3. Ancillary datasets

3.3.1 Water level, flood extent and volume

Our estimates were compared with the independent dataset made available by (“Impact of the Mekong River Flow Alteration on the Tonle Sap Flood Pulse,” 2008) over 1997-2005 consisting of annual minima and maxima water stages, inundation extent and volume. Water stages are from the Kampong Luong station located on the lakeshore. Kummu and Sarkkula (2008) used a Digital Bathymetric Model (DBM) to established polynomial relationships between stage and extent and stage and volume. The DBM was derived from the following three spatial sources: a hydrographic survey (MRC, 1999) to determine the contours of the lake and Tonle Sap River during the dry season; a survey map (Certeza Surveying, 1964) for delineating the Tonle Sap floodplain; and the Shuttle Radar Topography Mission data (“The Shuttle Radar Topography Mission,” 2007) for the surrounding areas to complete the DBM (see (“Water balance analysis for the Tonle Sap Lake-floodplain system,” 2014)for more details).

167

168 3.3.2 SRTM Digital Elevation Model (DEM)

169 The Shuttle Radar Topography Mission (SRTM) DEM was derived from the C and X Synthetic
170 Aperture Radar (SAR) images acquired for interferometry purposes on board the space shuttle
171 Endeavour from 11-22 February 2000 (Farr et al., 2007). In this study, the SRTM 1 Arc-Second (30
172 m) Global elevation data was used in the Tonle Sap watershed. This dataset is available from USGS
173 at: <https://eros.usgs.gov/elevation-products>.

174

175 3.3.3 TRMM/TMPA rainfall

176 The rainfall product used in this study is the Tropical Rainfall Measuring Mission (TRMM) Multi-
177 Satellite Precipitation Analysis (TRMM/TMPA) 3B43 v7 product. It is a combination of monthly
178 rainfall satellite data and other data sources at a spatial resolution of 0.25°. This dataset was derived by
179 combining satellite information from the TRMM Microwave Imager (TMI); the Precipitation Radar
180 (PR) and Visible and Infrared Scanner (VIRS) from the TRMM mission (operating from December
181 1997 to April 2015); the Special Sensor Microwave Imager (SSM/I) and Special Sensor Microwave
182 Imager/Sounder (SSM/I/S) on board some satellites of the US Air Force Defense Meteorological
183 Satellite Program (DMSP); the Advanced Microwave Scanning Radiometer – Earth Observing System
184 (AMSR-E, operating from June 2002 to October 2011) on board Aqua satellite; Advanced Microwave
185 Sounding Unit (AMSU) and Microwave Humidity Sounder (MHS) on board various meteorological
186 satellites (from 1998 to now); and rain gauge observations. The TRMM 3B43v7 product merges
187 TRMM 3B42-adjusted infrared precipitation with monthly accumulated precipitation from the Global
188 Precipitation Climatology Center (“The TRMM Multi-Satellite Precipitation Analysis (TMPA),”
189 2010) and is available on the Goddard Earth Sciences Data and Information Services Center (GES
190 DISC) website at: <https://mirador.gsfc.nasa.gov/>.

191

192 3.3.4 MODIS-based Global Land Cover Climatology

193 This climatology is based on the Collection 5.1 MODIS Land Cover Type (MCD12Q1) product at 500
194 m spatial resolution and obtained from analysis of MODIS images acquired between 2001 and 2010.
195 A re-analysis attributing a confidence score for each land cover type at each pixel was performed, as
196 substantial interannual variability in land cover types was found to affect 40% of the pixels. The final
197 land cover classification was obtained by choosing the type with the highest confidence score between
198 2001 and 2010 for each pixel (Broxton et al., 2014). This dataset is available from USGS at:
199 https://landcover.usgs.gov/global_climatology.php.

200 201 3.3.5. Climate indices

202 3.3.5.1 El Niño 3.4 Sea Surface Temperature index

203 El Niño Southern Oscillation (ENSO) oceanic indices are defined using Sea Surface Temperature
204 (SST) anomalies in different regions of the Pacific Ocean. El Niño 3.4 SST index is computed over a
205 region located in the eastern Pacific, between longitude 120° W and 170° W and latitude 5° N and 5°
206 S (“Global analyses of sea surface temperature, sea ice, and night marine air temperature since the late
207 nineteenth century,” 2003). It is available on a monthly time step starting from January 1870 at:
208 https://www.esrl.noaa.gov/psd/gcos_wgsp/Timeseries/Nino34/.

209 210 3.3.5.2 Pacific Decadal Oscillation index

211 The Pacific Decadal Oscillation (PDO) index is defined as the principal component of monthly SST
212 variability in the North Pacific, poleward of 20° N (“A Pacific Interdecadal Climate Oscillation with
213 Impacts on Salmon Production,” 1997). It is available on a monthly time step starting from January
214 1900 at: https://www.esrl.noaa.gov/psd/gcos_wgsp/Timeseries/PDO/.

215 216 3.3.5.3 Monsoon Indices

217 The Indian Monsoon Index (IMI) and the Western North Pacific Monsoon Index (WNPMI) are
218 defined as the difference of 850 hPa zonal wind over the areas (5°N–15°N, 40°E–80°E) and (20°N–

219 30°N, 70°E–90°E), (5°N–15°N, 100°E–130°E) and (20°N–30°N, 110°E–140°E), respectively,
220 between June and September (Wang and Fan, 1999); (“Interannual Variability of the Asian Summer
221 Monsoon,” 2001). It is available on a yearly time step from 1948 to 2015 at:
222 <http://apdrc.soest.hawaii.edu/projects/monsoon/seasonal-monidx.html>.

223

224 **4. Methods**

225 The lake and floodplain surface extent (section 4.1) and elevation (section 4.2) are first
226 estimated using MODIS and radar altimetry measurements, respectively. They are then
227 combined to compute the lake storage change (section 4.3). Finally, a rainfall standardized
228 anomaly index is computed (section 4.4) to investigate the link between this storage change
229 and rainfall.

230 4.1. Surface water extent

231 The approach developed by (Sakamoto et al., 2007) and simplified by Normandin et al., (2018) to
232 monitor flood extent in the Mekong Basin was applied to the Tonle Sap drainage area (processing
233 steps are presented in Figure S1 in the supplementary material section). It is based on the thresholding
234 of the Enhanced Vegetation Index (EVI), the Land Surface Water Index (LSWI), and the Difference
235 Value between EVI and LSWI (DVEL) to determine the status (non-flooded, mixture, flooded,
236 permanent water body) of any pixel in an 8-day composite MODIS image of surface reflectance.
237 These two spectral indexes were selected as the Short-wave infrared (SWIR) band is very sensitive to
238 soil and vegetation moisture content and because the Near infrared (NIR) band presents low surface
239 reflectance values over water bodies and high values over densely vegetated areas, whereas surface
240 reflectance values in the red band are higher for vegetation than over water bodies. Thus, these two
241 indexes are well suited to discriminate between water and vegetation.

242 The two indexes used in this approach are defined as follows (Huete, 1997):

$$243 \text{EVI} = 2.5 \times \frac{\rho_{\text{NIR}} - \rho_{\text{R}}}{\rho_{\text{NIR}} + 6 \times \rho_{\text{R}} - 7.5 \times \rho_{\text{B}} + 1} \quad (1)$$

$$LSWI = \frac{\rho_{NIR} - \rho_{SWIR}}{\rho_{NIR} + \rho_{SWIR}} \quad (2)$$

where ρ_{NIR} is the surface reflectance value in the near infrared (841-875 nm, band 2), ρ_R is the surface reflectance value in the red (621-670 nm, band 1), ρ_B the surface reflectance value in the blue (459-479 nm, band 3), and ρ_{SWIR} the surface reflectance in the short-wave infrared (1628-1652 nm, band 6). Following (Sakamoto et al., 2007), the approach summarized in Figure S1 for Normandin et al., (2018) was applied to the series of MODIS images. First, the pixels identified as cloud-covered were filtered out ($\rho_B \geq 0.2$). Then, a linear interpolation was performed to limit information loss over the study area. The pixels are classified into two major classes: non-flooded ($EVI > 0.3$ or $EVI \leq 0.3$ but $EVI - LSWI > 0.05$) and water-related pixels ($EVI \leq 0.3$ and $EVI - LSWI \leq 0.05$ or $EVI \leq 0.05$ and $LSWI \leq 0$). This latter class is divided into 3 subclasses: mixture pixels when $0.1 < EVI \leq 0.3$, flooded pixels $EVI \leq 0.1$, and long-term water bodies (e.g., rivers and lakes) when a pixel is determined flooded more than 250 days per year. Spatio-temporal variations of the flood were determined in the Tonle Sap drainage basin from February 2000 to December 2017.

4.2. Altimetry-based water levels

4.2.1 Post-processing of altimeter data

Radar altimetry was initially developed to provide accurate measurements of the sea surface topography and is now commonly used for the monitoring of inland water levels (see (Crétaux et al., 2017)2017 for a recent review). Variations of altimeter height from one cycle to another can be associated with water level changes.

In this study, we used the Multi-mission Altimetry Processing Software (MAPS) for processing altimetry data over land and ocean (e.g., (Frappart et al., 2015c); (Frappart et al., 2015a); (Biancamaria et al., 2017); Vu et al., 2018), that allows to build time-series of water levels at a virtual station (intersection between satellite track and water body), after a refined selection of the valid altimeter data. Data processing is composed of four main steps:

- 270 i) a rough delineation of the cross-section between the altimeter tracks and Tonle Sap using
271 Google Earth (Fig. 1b);
- 272 ii) loading of the altimetry over the study area and computation of altimeter heights from raw
273 data contained in the GDR;
- 274 iii) a refined selection of the valid altimetry data through visual inspection;
- 275 iv) computation of the water level time-series as the median of the selected water levels for each
276 cycle.

277 A detailed description of altimetry data processing using MAPS can be found in (Frappart et al.,
278 2015b). MAPS is available via CTOH. Previous studies have shown that Ice-1-derived altimetry
279 heights are the most suitable for hydrological studies in terms of water level accuracy and data
280 availability (e.g., (Frédéric Frappart et al., 2006); (F. Frappart et al., 2006); (Santos da Silva et al.,
281 2010)). They are among the commonly available retracked data in the GDR.

282 Measurement bias between missions and difference in satellite track locations were computed and
283 removed from each time series to obtain a consistent time series over the lake between all missions.
284 The final water elevation time series (in meters wrt EGM08 geoid) is computed with reference to
285 ENVISAT track 107 (the most eastward ENVISAT track on the lake, see Fig. 1b).

286

287 4.2.2 Specific processing of Topex-Poseidon and Jason time series

288 As shown in Figure 1b, Topex-Poseidon and Jason track over Tonle Sap Lake is very close to
289 its outlet. Consequently, and as visually observed on Landsat images, during low flow period the
290 observed area is representative of the Tonle Sap River, which connects the lake to the Mekong River,
291 whereas during high flow period it fully includes the lake extent. Correlation between Jason-2 time
292 series and ENVISAT over the period in common (more than 2 years) still remains high (0.9936), with
293 an RMSE of 0.23 m, after removing the common bias between the two time series. For low water
294 elevations (below 5.5 m), Jason-2 water elevations rise before those of ENVISAT and decrease later.
295 This could be due to hydraulic effects: water elevations vary differently in the lake and outlet river

296 because of bathymetry changes. To account for this observation in a simple way, we arbitrarily
297 considered that difference between the two time series can be corrected applying a time lag to Jason-2
298 time series, depending on the water elevations, to get a better match with ENVISAT time series. After
299 different tests on time lags and water elevation thresholds, the best correlation (0.9986) and lowest
300 RMSE between ENVISAT and Jason-2 (0.11 m) are obtained when Jason-2 water elevations below
301 5.5 m are delayed by 9 days, whereas water elevations above this threshold are delayed by 2 days.
302 More information on this issue is shown in Figures S2 to S4 in the supplementary information
303 section. The Topex-Poseidon, Jason-1 and Jason-3 time series used in this study are from the same
304 track and therefore the same processing has been applied (after removing the bias between these time
305 series and Jason-2 time series).

306

307 4.3. Surface water volume variations

308 MODIS-based flood extents were combined with altimetry-derived water levels to estimate
309 lake volume variations. Due to the extent of flooding in the watershed, our analysis was
310 limited to the pixels which are i) under water filling SRTM DEM with the water stage of the
311 lake (see the supplementary information, section 2, for method) and ii) connected to the lake
312 using a four-connected neighborhood. As flood extent is derived from a shorter time period
313 than water stage (1993-2017 instead of 2000-2017), a polynomial relationship between water
314 stage (h) and lake surface (S) was fitted to estimate surface water extent during the whole
315 altimetry period using Eq. 3:

$$316 S(h) = \sum_{i=1}^n a_i h^i \quad (3)$$

317 where a_i is the coefficient of degree i of the polynomial and n the maximum degree of the
318 polynomial. A confidence interval of 95%, a RSME of 74 km² and R² of 0.99 were found
319 using a second degree polynomial with the following values: $a_0=6013.0$ km², $a_1=-1518.0$ km
320 and $a_2=-176.9$. As in Baup et al. (2014) or Crétaux et al. (2015; 2016), the volume variations
321 of the lake (ΔV), between two consecutive time steps ($t-1$ and t) were estimated using the

322 assumption of a regular morphology of the lake and a pyramidal shape:

$$323 \Delta V = \frac{(h(t)-h(t-1))(S(t)+S(t-1))+\sqrt{S(t)S(t-1)}}{3} \quad (4)$$

324

325 4.4. Standardized Precipitation Anomaly Index

326 The Standardized Precipitation Anomaly Index (SPAI) was defined by (Lamb, 1982) to study
327 interannual rainfall variations:

$$328 I_R(t) = \frac{1}{n} \sum_{i=1}^n \frac{R(i,t) - \langle R(i,\tau) \rangle_{\tau \in T}}{\sigma(R(i,\tau))_{\tau \in T}} \quad (5)$$

329 where $R(i,t)$ is the annual rainfall at TRMM 3B43v7 gridpoint i for hydrological year t ,
330 $\langle R(i,\tau) \rangle_{\tau \in T}$ and $\sigma(R(i,\tau))_{\tau \in T}$ are the annual average and standard deviation over the
331 reference period T at gridpoint i , respectively, and n is the total number of gridpoints in the
332 study area. The hydrological year is defined between November of year $t-1$ and October of
333 year t .

334

335 5. Results and discussion

336 5.1. Validation of surface water extent and storage

337

338 Variations of lake surface extent were estimated between February 2000 and December 2017
339 by applying the threshold approach to MODIS images. The average number of days per year
340 with missing data due to cloud presence were computed for each pixel, as well as the
341 associated standard deviation over the whole study period (see Fig. S5 in supplementary
342 information). The annual lack of data due to cloud presence over Tonle Sap Lake and its
343 floodplains is generally less than 8 days (1 image) and can reach up to 24 days (3 images),
344 with standard deviations less than 16 days (2 images). This lack of data (not occurring on
345 consecutive dates) does not prevent the use of MODIS images for monitoring Tonle Sap
346 seasonal flooding. Maps of annual average duration of inundation extent and associated

347 standard deviation are presented in Figures 2a and 2b, respectively, along with maximum and
348 minimum inundation extents during the flood peak in 2011 (Figs. 2c) and 2015 (Figs. 2d),
349 respectively, considering only pixels classified as inundated. Fig. 3 is similar to Fig. 2, but
350 uses both pixels classified as inundated and the ones classified as mixed pixel. Extensive
351 inundation is generally in the western part of the lake during time spans shorter than 3
352 months, but can also occur in the eastern part of the lake and along its north to south flowing
353 tributary in the eastern part of the basin. Longer inundation, lasting between 4 and 5 months
354 but of smaller extent, can be observed in the lake's outlet and also in the northeastern part
355 (Fig. 2a). These inundations are characterized by a large interannual variability with standard
356 deviations between 40 and 50 days (Fig. 2b). In 2011, important inundations (>100 days)
357 were observed in all eastern and northwestern parts of the lake (Fig. 2c), whereas almost no
358 flooding was detected in 2015 (Fig. 2d). In addition, considering the mixed pixels (i.e., the
359 pixels partly inundated), the patterns are similar to those presented in Fig. 2, but with a larger
360 extent and longer presence (Fig. 3). Floods lasting up to 6 months were detected in the
361 western parts of the lake (Figs. 3a and 3c), and are in good agreement with results from
362 previous studies (Kummu and Sarkkula, 2008; Arias et al., 2012; Kummu et al., 2014). Large
363 differences were obtained between the flood extent using only the flooded pixels and using
364 both the flooded and mixed pixels in terms of maximum extent and flood duration inside the
365 maximum inundation extent defined filling SRTM DEM with altimetry-based water stage
366 (Fig. S6). Even if SRTM DEM exhibits a high frequency noise (variations of 1 or 2 m from
367 one pixel to another, see Fig. S7), large-scale elevation variations are well retrieved
368 considering the minimum elevation in the MODIS pixels (Fig. S8) and do not prevent its use
369 for determining temporal variations of maximum flood extent. In the following, surface water
370 extents were obtained by considering both the flooded and mixed pixels which are i) under
371 water filling SRTM DEM with the water stage of the lake and ii) connected to the lake using a
372 four-connected neighborhood.

373 Figure 4a presents temporal variations of surface water extent in the Tonle Sap drainage
374 basin between February 2000 and December 2017 using MODIS images. They exhibit a well-
375 marked seasonal cycle, with minima occurring in April and May and maxima between
376 September and November. There is a strong interannual variability of the maximum flood
377 extent ranging from 5,114 km² in October 2015 up to 13,736 km² in October 2011. The
378 minimum lake surface varies between 2,320 km² in 2016 and 2,800 km² in 2000 during low
379 stage. Water stage changes accordingly, with an annual amplitude (i.e. difference between the
380 maximum and the minimum over the year) varying from 5.5 m in 2015 to 9 m in 2011 (Fig.
381 4b), resulting in volume variations of Tonle Sap lake that range from 31 km³ in 2015 to 101
382 km³ in October 2000 and 2011 (Fig. 4c). Comparisons were made using annual amplitude of
383 the lake water stage, inundated surface in the Tonle Sap basin, and water volume estimated by
384 Kumm and Sarkkula (2008) using a Digital Bathymetric Model (DBM) and in situ water
385 levels, over the common period of availability of the different datasets (i.e., 1997-2005 for
386 water stages and volumes, and 2000-2005 for inundated surfaces). A very good agreement
387 was found (in terms of annual amplitude) between altimetry-based and in situ water levels
388 ($R=0.97$, $RMSE=0.27$ m and $RRMSE=3.5\%$), and multi-satellite-derived and Kumm and
389 Sarkkula (2008) water volume variations ($R=0.96$, $RMSE=12$ km³ and $RRMSE=19\%$). A
390 good agreement was also found between MODIS-based and Kumm and Sarkkula (2008)
391 surface water extent ($R=0.89$, $RMSE=982$ km² and $RRMSE=9.9\%$). If the very good
392 agreement between in situ and altimetry-based water levels can confirm observations from
393 Topex/Poseidon in a previous study with a $RMSE$ of 0.23 cm (Frappart et al., 2006b), the
394 small discrepancies observed in surface water extent and volume can be attributed to
395 differences of approach in Kumm and Sarkkula (2008) and our own study. The composite
396 DBM including old measurements of the floodplain's topography is liable to introduce some
397 errors to Kumm and Sarkkula's (2008) approach, whereas the delineation of inundation
398 extent using images at the moderate resolution of 500 m and the SRTM DEM is responsible

399 for overestimation of the flooded area due to the presence of mixed pixels. Nevertheless, both
400 approaches present very consistent results and can be used to estimate water balance in the
401 drainage area.

402 Over the study period, interannual variations of surface water volume were computed from
403 monthly lake water volume with the removal of monthly climatological averages. The range
404 is between -35.99 km^3 in 2015 to 35.53 km^3 in 2000 (Fig. 5a). The variations were compared
405 with SPAI (see section 4.4) from TRMM/TMPA 3B43 averaged over the Tonle Sap
406 watershed and over the entire Mekong Basin from 1998-2017 (Fig. 5b). Correlation
407 coefficients between the interannual variations of surface water volume and SPAI (defined
408 during the hydrological year between November of year n-1 and October of year n) are equal
409 to 0.61 (p-value= $5.1 \cdot 10^{-3}$) and 0.77 (p-value= 10^{-4}) for the Tonle Sap watershed and the
410 Mekong Basin, respectively. These results are related to the hydrological regime of the Tonle
411 Sap watershed, whose flood pulse is driven by the flow of the Mekong River. Annual
412 precipitation anomalies can account for the large droughts of 1998, 2010 and 2015 and large
413 floods of 2000, 2001 and 2011 with SPAI lower than -1 and higher than 1, respectively, for
414 both the Tonle Sap watershed and the Mekong Basin, but cannot explain the large flood of
415 2002 and large drought of 2016 according to TRMM/TMPA 3B43 dataset. Similar
416 comparisons were performed during the dry and rainy seasons. Correlation coefficients were
417 found equal to 0.31 (p-value=0.19) and 0.84 (p-value close to 0) during the dry and rainy
418 seasons, respectively, for the Mekong Basin and to 0.45 (p-value= $4.5 \cdot 10^{-2}$) and 0.58 (p-
419 value= $7.5 \cdot 10^{-3}$) during the dry and rainy seasons, respectively, for the Tonle Sap watershed.
420 These results confirm that surface water volume of the Tonle Sap watershed is strongly
421 influenced by rainfall during the rainy seasons in the Mekong Basin. During the large flood
422 events of 2000, 2001 and 2011, SPAI during the rainy season of between 1 and 1.5 were
423 obtained in the whole Mekong Basin (Fig. 5c). Larger floods were recorded in 2000 and 2011
424 as they were enhanced by SPAI between 1 and 1.5 in the Tonle Sap watershed. A very low

425 positive SPAI was observed in the Tonle Sap watershed during the wet season of 2001.
426 However, high positive anomalies (~ 2) were observed in the dry season and contributed to the
427 excess in surface water storage for the same year (see Fig.5d). This was also observed in the
428 year 2000, which was the largest flood between 1995 and 2016. Inverse conclusions can be
429 made for the large droughts of 1998, 2010 and 2015 with SPAI between -1.5 and -2 (Fig. 5c)
430 during the wet season. Lower rainfall during the dry season seems to have a low impact as
431 small anomalies were observed during the lowest drought in 2015 (Fig. 5d). The 2002 flood
432 was higher than that of 2001 in spite of a much lower positive SPAI. This was due to a higher
433 than usual lake level at the beginning of the 2002 hydrological year. Conversely, low rainfall
434 deficit was responsible for low water surface storage in 2016 due to the very low lake level at
435 the end of the 2015 hydrological year. For a comparison, the anomaly of lake water volume
436 was 6.8 km^3 in December 2001 and -21.9 km^3 in December 2015. In addition, daily in-situ
437 data of water levels recorded at the Prek Kdam station in the Tonle Sap River (which joins the
438 Mekong River to Tonle Sap Lake) are displayed on the Mekong River Commission website
439 during both dry and flood seasons since 2013 (ffw.mrcmekong.org/historical_rec.htm). A
440 visual inspection showed very similar water stage amplitude between in situ and altimetry
441 time series. Extreme events were defined by considering deviations larger (lower) than two
442 thirds of the maximum (minimum) estimated over the observation period (i.e., around ± 24
443 km^3). Four positive and three negative extrema can be observed. For positive extrema:
444 between July and November 2000, peaking at 36.36 km^3 in September 2000; 24.22 km^3 in
445 September 2001; in September and October 2002, peaking at 35.37 km^3 in September 2002;
446 and in September and October 2011, peaking at 30.77 km^3 in October 2011. For negative
447 extrema: between September and November 1998, peaking at -31.42 km^3 in October 1998;
448 between September and November 2015, peaking at -36.07 km^3 in October 2015; and -24.22
449 km^3 in September 2011 (Fig. 6a). In the following, we compare these exceptional droughts
450 and floods to climatic indexes to see if they are related to climate variability.

5.2. Surface water storage and climate variability

Positive anomalies of surface water volume in the Tonle Sap watershed in September-October correspond to negative values of ENSO3.4 index defined by Rayner (2003) (Fig. 6b). On the contrary, negative anomalies of surface water volume in the watershed correspond to positive values of ENSO 3.4. Larger anomalies occur when ENSO index and the Pacific Decadal Oscillation (PDO) index (as defined by Mantua et al (1997)) exhibit large deviations and are in phase. Large positive (respectively negative) anomalies of the lake volume are obtained for moderate (between 1 and 1.5 °C) to very strong (above 2°C) negative (respectively positive) values of both ENSO (El Niño, respectively La Niña, Fig. 6b) and PDO (Fig. 6c) during the previous winter. This phenomenon is caused by a significant intensification of the negative relationship between ENSO and the monsoon when ENSO and PDO are in phase. It was previously described regarding the East Asian monsoon (Kim et al., 2014). Positive values of ENSO and PDO are associated with anomalous warm temperature patterns over East Asia that cause rainfall deficit the following summer. Negative values of ENSO and PDO are linked with anomalous cold temperature patterns, leading to excess rainfall the following summer. On the contrary, when ENSO and PDO are out of phase, interannual variations are lower. The super strong ENSO event in 2015/2016 was an exception, as it did not result in huge rainfall in either the Tonle Sap watershed or the Mekong Basin. This was most likely due to its rapid decay in boreal spring 2016 causing a weakening of the western Pacific subtropical anticyclone (Liu et al., 2017). Correlation between annual amplitude of volume variations and climatic indices were also estimated, and several time-periods were tested. Stronger correlations were found when the ENSO index was averaged over December to February (DJF) as in Räsänen and Kummu (2013) and when the PDO index was averaged over November to March (NDJFM) as in Newman et al., (2003). For $ENSO_{DJF}$, $R=-0.70$ with a p-value equal to 10^{-4} , whereas for PDO_{NDJFM} , $R=-0.68$ with a p-value equal to 2.10^{-4} . This confirms earlier findings about relationships in the Mekong Basin between rainfall, discharge,

477 ENSO (Räsänen and Kummu, 2013) and PDO (Delgado et al., 2012). An even higher
478 correlation was found between annual anomalies of surface water storage and ENSO 3.4
479 index than between annual flow and ENSO 3.4 (Räsänen and Kummu, 2013) and this study
480 provides a quantification of the relationship between flood pulse and PDO in the Mekong
481 Basin. The optimal least-squares linear combination of both indices provides a correlation of -
482 0.75. The coefficients of this linear combination are equal to 1.0 and 0.84 for ENSO 3.4 and
483 PDO, respectively. Time series of annual amplitude of lake volume (Fig. 7a), of the ENSO
484 3.4 index averaged over DJF (Fig. 7b) and of the PDO index averaged over NDJFM (Fig. 7c)
485 illustrate differences in the impact of extreme events on lake volume. The drought of 1998
486 and the floods of 2000 and 2011 are directly related to large positive and negative anomalies
487 of both ENSO 3.4 and PDO. The 2002 flood and 2015/2016 droughts can be attributed to both
488 a large value in module of either ENSO 3.4 or PDO (and a lower value of the other index),
489 and the existence of an excess (since 2000) or a deficit (since 2014) of water in the lake. This
490 shows that the possibility of occurrence of a hydrological extreme is not only conditioned by
491 climate factors but also by base water storage from previous years.

492 We propose to quantify the monsoonal impact on lake storage, as the flood pulse in the
493 Mekong Basin is driven by the monsoon. The Mekong Basin is under the influence of both
494 the Indian and the Western North Pacific Monsoons (Delgado et al., 2012). Correlation
495 between anomalies of annual surface water storage and Western North Pacific Monsoons
496 (WNPPI, Wang et al., 2001) and Indian Monsoon (IMI, Wang and Fan 1999) provides better
497 results ($R=0.55$, $p\text{-value}=0.006$, and $R=0.49$, $p\text{-value}=0.018$) for July and August,
498 respectively. This is similar to the relationship between water discharge and WNPPI in the
499 downstream Mekong Basin discovered by Delgado et al., (2012).

500

501 5.3) Impact of the 2015 extreme drought on vegetation activity

502 Vegetation activity is highly related to flood duration (Arias et al., 2013). In the following,

503 impact of the 2015 drought on the Tonle Sap ecosystem is analyzed using MODIS-derived
504 EVI time series and a land cover map. The 1998 and 2015 extreme droughts were the worst
505 observed during the study period, but MODIS images are only available since February 2000.
506 Due to this, our analysis is limited to the 2015 drought. Figure 8a shows land cover types
507 from the 500 m MODIS-based Global Land Cover Climatology (Broxton et al., 2014) for the
508 Tonle Sap Basin. Time series of Enhanced Vegetation Index (EVI) and their interannual
509 variations (estimated by removing the climatological monthly mean to the monthly values)
510 were computed for each land cover type. In the following, only land cover types
511 corresponding to vegetation are considered. They are presented for the three main land cover
512 types which cover 80.3% of the Tonle Sap basin surface (Evergreen Broadleaf Forest,
513 Woody Savannas and Cropland/Natural Vegetation Mosaic) as seen in Figures 8b and c for
514 the time series and associated anomalies, respectively, and in Figures S9a and b for the five
515 other classes of vegetation which cover 14.6% of the surface of the Tonle Sap Basin surface
516 (Mixed Forests, Savannas, Grasslands, Permanent Wetlands and Croplands). Lower than
517 usual minimum values of EVI are observed in spring 2016 for all land cover types as shown
518 in Figures 8b and S9a. The anomalies reached their lowest values in April 2016 for Evergreen
519 Broadleaf Forest, Woody Savannas and Cropland/Natural Vegetation Mosaic with EVI
520 anomalies of -0.11, -0.13 and -0.06 (Fig. 8c), corresponding to an annual variation of
521 amplitude around 0.10, 0.25 and 0.15, respectively. The same timing is observed for
522 Savannas, Grasslands and Permanent Wetland with EVI anomalies of -0.10, -0.05 and -0.12
523 (Fig. S9b), corresponding to an annual variation of amplitude around 0.25, 0.10 and 0.30,
524 respectively. They reached their lowest values in May 2016 for Mixed Forests and Croplands
525 with EVI anomalies of -0.15 and -0.04 (Fig. S9b), corresponding to annual variation of
526 amplitude around 0.10 and 0.15, respectively. The spatial distribution of anomalies of EVI for
527 April and May are presented in Figures 9a and 9b, respectively. They are quite similar to
528 lowest anomaly values in April 2016. The largest negative anomalies are located on the

529 Woody Savannas in the northeast and southwest of the watershed, as well as on the Evergreen
530 Broadleaf Forest located in the east and southwest, and the grasslands of the downstream part.
531 Croplands were generally less affected thanks to irrigation. Some rare positive anomalies
532 were also found around the lake. For instance, the extreme drought of 2015 modified
533 vegetation activity during the first semester of 2016. The temporal evolution of EVI of the
534 Evergreen Broadleaf Forest, Woody Savannas and Cropland/Natural Vegetation Mosaic (Fig.
535 10) as well as Savannas, Grasslands and Croplands (Fig. S10) exhibit a longer and lower than
536 usual period of low activity (until June instead of April) where it presents minimum activity
537 between January and June instead of a maximum for Mixed Forests and Wetlands (Fig. S10).
538 Normal and even slightly above normal EVI values are found for the rest of 2016 and also for
539 2017 (Figs. 8b, 8c, S9a and S9b).

541 **6. Conclusion**

542 Surface water storage variations of Tonle Sap were determined combining remotely sensed
543 inundation extent data derived from MODIS reflectance images and altimetry-based water
544 levels from 1993-2017. Their interannual anomalies were found to be more related to the
545 rainfall occurring in the Mekong Basin ($R=0.77$ for the interannual variations during the
546 whole hydrological year) than in the Tonle Sap watershed ($R=0.61$) as flooding in the Tonle
547 Sap watershed is mostly driven by the flow of Mekong River. Nevertheless, extreme events
548 (exceptional floods and droughts) occurred when large excess/deficit rainfall occurred during
549 the rainy season in both the Mekong Basin ($R=0.84$) and Tonle Sap watershed ($R=0.58$).
550 Excess rainfall occurring in both dry and rainy seasons in the Mekong Basin combined with a
551 rainfall deficit in the Tonle Sap watershed during the rainy season was only seen to cause
552 large flooding in 2001. Important memory effects were also detected as in the extreme flood
553 of 2002. This was mostly due to excess in surface water storage of the exceptional flood of
554 2000 and the large flood in 2001, whereas the extreme drought of 2016 was caused by the

555 deficit in surface water by the drought of 2014 and the extreme drought of 2015. A quasi-
556 equal influence of the West North Pacific and Indian Monsoons was also found with
557 correlations between the interannual variations of surface water storage and the WNPMI in
558 July of 0.55 and the IMI in August of 0.49.

559 Interannual variations of surface water storage in the Tonle Sap watershed are strongly
560 influenced by climate variability. They exhibit large positive and negative anomalies
561 corresponding to extreme drought (1998, 2015, and 2016) and flood (2000, 2001, 2002, and
562 2011) events. They were related to the very strong El Niño events of 1997-1998 and 2015-
563 2016 and the moderate La Niña events of 1999-2000 and 2010-2011 enhanced by the PDO.
564 Correlation coefficients between the interannual variations of surface water storage of the
565 Tonle Sap watershed and the average ENSO 3.4 index over DJF and PDO over NDJFM were
566 found equal to -0.70 and -0.68, respectively. R of -0.75 was found using a linear combination
567 of the two former indices. Below normal EVI values for the types of vegetation were
568 observed in the first semester of 2016 as a consequence of the 2015 drought.

569 The NASA/CNES Surface Water and Ocean Topography (SWOT) mission is to be launched
570 in 2021 and will improve flood monitoring in Tonle Sap by providing water level maps
571 through SAR interferometry techniques at better spatial and temporal resolutions with low
572 impact of cloud presence and vegetation. The data will provide a better understanding of the
573 strong relationship between climatic indices and Tonle Sap lake volume extreme changes,
574 suggested by Räsänen and Kummu (2013) for the whole Mekong basin and therefore help in
575 forecasting the risk of extreme droughts or floods.

577 **7. Acknowledgements**

578 This work was supported by the CNES, through TOSCA grants attributed to the "Variabilité
579 hydro-sédimentaire du bassin hydrologique du MEKONG par télédétection

(VolTransMesKong)" project and to the "Centre de Topographie de l'Océan et de l'Hydrosphère (CTOH)". It is based on observations with nadir radar altimeters on board Topex/Poseidon, Jason-1, Jason-2, Jason-3, ERS-2, ENVISAT, and SARAL satellites and with MODIS instruments on board Terra and Aqua satellites. C. Normandin is supported by a PhD grant from Ministère de l'Enseignement Supérieur et de la Recherche. The Mekong River Commission (MRC) is also warmly thanked for providing on its website (www.mrcmekong.org) many resources concerning the Mekong basin. We thank Dr. S. Calmant, Dr. J.-F. Crétaux and two anonymous reviewers for their very useful comments that helped improve this manuscript.

8. References

- Adrian, R., O'Reilly, C.M., Zagarese, H., Baines, S.B., Hessen, D.O., Keller, W., Livingstone, D.M., Sommaruga, R., Straile, D., Van Donk, E., Weyhenmeyer, G.A., Winder, M., 2009. Lakes as sentinels of climate change. *Limnol. Oceanogr.* 54, 2283–2297. doi:10.4319/lo.2009.54.6_part_2.2283
- Arias, M.E., Cochrane, T.A., Kummu, M., Lauri, H., Holtgrieve, G.W., Koponen, J., Piman, T., 2014. Impacts of hydropower and climate change on drivers of ecological productivity of Southeast Asia's most important wetland. *Ecol. Model.* 272, 252–263. doi:10.1016/j.ecolmodel.2013.10.015
- Arias, M. E., Cochrane, T. A., Norton, D., Killeen, T. J., Khon, P., 2013. The flood pulse as the underlying driver of vegetation in the largest wetland and fishery of the Mekong Basin. *Ambio*, 42(7), 864-876, doi: 10.1007/s13280-013-0424-4
- Arias, M.E., Cochrane, T.A., Piman, T., Kummu, M., Caruso, B.S., Killeen, T.J., 2012. Quantifying changes in flooding and habitats in the Tonle Sap Lake (Cambodia) caused by water infrastructure development and climate change in the Mekong Basin. *J. Environ. Manage.* 112, 53–66. doi:10.1016/j.jenvman.2012.07.003
- Baup, F., Frappart, F., Maubant, J., 2014. Combining high-resolution satellite images and altimetry to estimate the volume of small lakes. *Hydrol. Earth Syst. Sci.* 18, 2007–2020. doi:10.5194/hess-18-2007-2014
- Biancamaria, S., Frappart, F., Leleu, A.-S., Marieu, V., Blumstein, D., Desjonquères, J.-D., Boy, F., Sottolichio, A., Valle-Levinson, A., 2017. Satellite radar altimetry water elevations performance over a 200 m wide river: Evaluation over the Garonne River. *Adv. Space Res.* 59, 128–146. doi:10.1016/j.asr.2016.10.008
- Broxton, P.D., Zeng, X., Sulla-Menashe, D., Troch, P.A., 2014. A Global Land Cover Climatology Using MODIS Data. *J. Appl. Meteor. Climatol.* 53, 1593-1605. doi:10.1175/JAMC-D-13-0270.1
- Campbell, I.C., Poole, C., Giesen, W., Valbo-Jorgensen, J., 2006. Species diversity and ecology of Tonle Sap Great Lake, Cambodia. *Aquat. Sci.* 68, 355–373. doi:10.1007/s00027-006-0855-0
- Campbell, I.C., Say, S., Beardall, J., 2009. Chapter 10 - Tonle Sap Lake, the Heart of the

- 619 Lower Mekong, in: *The Mekong*. Academic Press, San Diego, pp. 251–272.
- 620 Certeza Surveying. 1964. Final Report to the Committee for Coordination of Investigations of the
- 621 Lower Mekong Basin. Certeza, Quezon City, The Philippines.
- 622 Crétaux, J.-F., Abarca-del-Río, R., Bergé-Nguyen, M., Arsen, A., Drolon, V., Clos, G.,
- 623 Maisongrande, P., 2016. Lake Volume Monitoring from Space. *Surv. Geophys.* 37, 269–
- 624 305. doi:10.1007/s10712-016-9362-6
- 625 Crétaux, J.-F., Nielsen, K., Frappart, F., Papa, F., Calmant, S., Benveniste, J., 2017.
- 626 Hydrological applications of satellite altimetry: rivers, lakes, man-made reservoirs,
- 627 inundated areas., in: Stammer, D., Cazenave, A. (Eds.), *Satellite Altimetry Over Oceans*
- 628 *and Land Surfaces, Earth Observation of Global Changes*. CRC Press.
- 629 Crétaux, J.-F., Biancamaria, S., Arsen, A., Bergé-Nguyen, M., Becker, M., 2015. Global
- 630 surveys of reservoirs and lakes from satellites and regional application to the Syrdarya
- 631 river basin. *Environ. Res. Lett.* 10, 015002. doi:10.1088/1748-9326/10/1/015002
- 632 Cruz, R.V., Harasawa, H., Lal, M., Wu, S., Anokhin, Y., Punsalmaa, B., Honda, Y., Jafari,
- 633 M., Li, C., Huu Ninh, N., 2007. *Asia. Climate Change 2007: Impacts, Adaptation and*
- 634 *Vulnerability. Contribution of Working Group II to the Fourth Assessment Report of the*
- 635 *Intergovernmental Panel on Climate Change*, Parry, M.L., Canziani, O.F., Palutikof, J.P.,
- 636 van der Linden, P.J., Hanson, C.E. Eds., Cambridge University Press, Cambridge, UK,
- 637 469-506
- 638 Delgado, J.M., Merz, B., Apel, H., 2012. A climate-flood link for the lower Mekong River.
- 639 *Hydrol. Earth Syst. Sci.* 16, 1533–1541. doi:10.5194/hess-16-1533-2012
- 640 Farr, T.G., Rosen, P.A., Caro, E., Crippen, R., Duren, R., Hensley, S., Kobrick, M., Paller,
- 641 M., Rodriguez, E., Roth, L., Seal, D., Shaffer, S., Shimada, J., Umland, J., Werner, M.,
- 642 Oskin, M., Burbank, D., Alsdorf, D., 2007. The Shuttle Radar Topography Mission. *Rev.*
- 643 *Geophys.* 45. doi:10.1029/2005RG000183
- 644 Fayne, J.V., Bolten, J.D., Doyle, C.S., Fuhrmann, S., Rice, M.T., Houser, P.R., Lakshmi, V.,
- 645 2017. Flood mapping in the lower Mekong River Basin using daily MODIS observations.
- 646 *Int. J. Remote Sens.* 38, 1737–1757. doi:10.1080/01431161.2017.1285503
- 647 Frappart, F., Calmant, S., Cauhopé, M., Seyler, F., Cazenave, A., 2006a. Preliminary results
- 648 of ENVISAT RA-2-derived water levels validation over the Amazon basin. *Remote Sens.*
- 649 *Environ.* 100, 252–264. doi:10.1016/j.rse.2005.10.027
- 650 Frappart, F., Fatras, C., Mougin, E., Marieu, V., Diepkilé, A.T., Blarel, F., Borderies, P.,
- 651 2015a. Radar altimetry backscattering signatures at Ka, Ku, C, and S bands over West
- 652 Africa. *Phys. Chem. Earth Parts ABC* 83–84, 96–110. doi:10.1016/j.pce.2015.05.001
- 653 Frappart, F., Legrésy, B., Niño, F., Blarel, F., Fuller, N., Fleury, S., Birol, F., Calmant, S.,
- 654 2016. An ERS-2 altimetry reprocessing compatible with ENVISAT for long-term land and
- 655 ice sheets studies. *Remote Sens. Environ.* 184, 558–581. doi:10.1016/j.rse.2016.07.037
- 656 Frappart, F., Minh, K.D., L’Hermitte, J., Cazenave, A., Ramillien, G., Le Toan, T., Mognard-
- 657 Campbell, N., 2006. Water volume change in the lower Mekong from satellite altimetry
- 658 and imagery data. *Geophys. J. Int.* 167, 570–584. doi:10.1111/j.1365-246X.2006.03184.x
- 659 Frappart, F., Papa, F., Marieu, V., Malbeteau, Y., Jordy, F., Calmant, S., Durand, F., Bala, S.,
- 660 2015b. Preliminary Assessment of SARAL/AltiKa Observations over the Ganges-
- 661 Brahmaputra and Irrawaddy Rivers. *Mar. Geod.* 38, 568–580.
- 662 doi:10.1080/01490419.2014.990591
- 663 Frappart, F., Roussel, N., Biancale, R., Martinez Benjamin, J.J., Mercier, F., Perosanz, F.,
- 664 Garate Pasquin, J., Martin Davila, J., Perez Gomez, B., Gracia Gomez, C., Lopez Bravo,
- 665 R., Tapia Gomez, A., Gili Ripoll, J., Hernandez Pajares, M., Salazar Lino, M., Bonnefond,
- 666 P., Valles Casanova, I., 2015c. The 2013 Ibiza Calibration Campaign of Jason-2 and
- 667 SARAL Altimeters. *Mar. Geod.* 38, 219–232. doi:10.1080/01490419.2015.1008711
- 668 Hortle, K.G., 2007. Consumption and the Yield of Fish and Other Aquatic Animals from the
- 669 Lower Mekong Basin. MRC Technical Paper No16, Mekong River Commission,

670 Vientiane. 87 pp. ISSN: 1383-1489.

671 Huete, A., 1997. A comparison of vegetation indices over a global set of TM images for EOS-

672 MODIS. *Remote Sens. Environ.* 59, 440–451. doi:10.1016/S0034-4257(96)00112-5

673 Huffman, G.J., Adler, R.F., Bolvin, D.T., Nelkin, E.J., 2010. The TRMM Multi-Satellite

674 Precipitation Analysis (TMPA), in: Gebremichael, M., Hossain, F. (Eds.), *Satellite Rainfall*

675 *Applications for Surface Hydrology*. Springer Netherlands, Dordrecht, pp. 3–22.

676 doi:10.1007/978-90-481-2915-7_1

677 Junk, W.J., Brown, M., Campbell, I.C., Finlayson, M., Gopal, B., Ramberg, L., Warner, B.G.,

678 2006. The comparative biodiversity of seven globally important wetlands: a synthesis.

679 *Aquat. Sci.* 68, 400–414. doi:10.1007/s00027-006-0856-z

680 Kamoshita, A., Ouk, M., 2015. Field level damage of deepwater rice by the 2011 Southeast

681 Asian Flood in a flood plain of Tonle Sap Lake, Northwest Cambodia. *Paddy Water*

682 *Environ.* 13, 455–463. doi:10.1007/s10333-014-0463-x

683 Kim, J.-W., Yeh, S.-W., Chang, E.-C., 2014. Combined effect of El Niño-Southern

684 Oscillation and Pacific Decadal Oscillation on the East Asian winter monsoon. *Clim. Dyn.*

685 42, 957–971. doi:10.1007/s00382-013-1730-z

686 Kummu, M., Sarkkula, J., 2008. Impact of the Mekong River Flow Alteration on the Tonle

687 Sap Flood Pulse. *AMBIO J. Hum. Environ.* 37, 185–192. doi:10.1579/0044-

688 7447(2008)37[185:IOTMRF]2.0.CO;2

689 Kummu, M., Sarkkula, J., Koponen, J., Nikula, J., 2006. Ecosystem Management of the Tonle

690 Sap Lake: An Integrated Modelling Approach. *Int. J. Water Resour. Dev.* 22, 497–519.

691 doi:10.1080/07900620500482915

692 Lamb, P.J., 1982. Persistence of Subsaharan drought. *Nature* 299, 46–48. doi:10.1038/299046a0

693 Lamberts, D., 2006. The Tonle Sap Lake as a Productive Ecosystem. *Int. J. Water Resour.*

694 *Dev.* 22, 481–495. doi:10.1080/07900620500482592

695 Lemoalle, J., Bader, J.-C., Leblanc, M., Sedick, A., 2012. Recent changes in Lake Chad:

696 Observations, simulations and management options (1973–2011). *Glob. Planet. Change*

697 80–81, 247–254. doi:10.1016/j.gloplacha.2011.07.004

698 Lim, P., Lek, S., Touch, S.T., Mao, S.-O., Chhouk, B., 1999. Diversity and spatial distribution

699 of freshwater fish in Great Lake and Tonle Sap river (Cambodia, Southeast Asia). *Aquat.*

700 *Living Resour.* 12, 379–386. doi:10.1016/S0990-7440(99)00107-2

701 Liu, B., Zhu, C., Su, J., Hua, L., Duan, Y., 2017. Why was the western Pacific subtropical

702 anticyclone weaker in late summer after the 2015/2016 super El Niño?: WEAKENED

703 WPSA FOLLOWING THE 2015/2016 SUPER EL NIÑO. *Int. J. Climatol.*

704 doi:10.1002/joc.5160

705 Lu, X.X., Li, S., Kummu, M., Padawangi, R., Wang, J.J., 2014. Observed changes in the

706 water flow at Chiang Saen in the lower Mekong: Impacts of Chinese dams? *Quat. Int.* 336,

707 145–157. doi:10.1016/j.quaint.2014.02.006

708 Magnuson, J.J., 2000. Historical Trends in Lake and River Ice Cover in the Northern

709 Hemisphere. *Science* 289, 1743–1746. doi:10.1126/science.289.5485.1743

710 Mantua, N.J., Hare, S.R., Zhang, Y., Wallace, J.M., Francis, R.C., 1997. A Pacific

711 Interdecadal Climate Oscillation with Impacts on Salmon Production. *Bull. Am. Meteorol.*

712 *Soc.* 78, 1069–1079. doi:10.1175/1520-0477(1997)078<1069:APICOW>2.0.CO;2

713 MRC, 1999. *Hydrographic Atlas of 1999 for the Tonle Sap River and the Tonle Sap Lake.*

714 Mekong River Commission (MRC), Phnom Penh, Cambodia.

715 MRC, 2003. *State of the Basin Report: 2003.* Mekong River Commission, Phnom Penh,

716 Cambodia. 316 pp. ISSN: 1728–3248.

717 MRC, 2005. *Overview of the Hydrology of the Mekong Basin.* Mekong River Commission,

718 Vientiane, November 2005; 82.

719 MRCS/WUP-FIN, 2006. *Technical Paper No. 5 - Tonle Sap Lake Water Balance*

720 *Calculations, WUP-FIN Phase II - Hydrological, Environmental and Socio-Economic*

721 Modeling Tools for the Lower Mekong Basin Impact Assessment. Mekong River
722 Commission and Finnish Environment Institute Consultancy Consortium, Vientiane, Lao
723 PDR, 32 pp.

724 Newman, M., Compo, G.P., Alexander, M.A., 2003. ENSO-Forced Variability of the Pacific
725 Decadal Oscillation. *J. Clim.* 16, 3853–3857. doi:10.1175/1520-
726 0442(2003)016<3853:EVOTPD>2.0.CO;2

727 Normandin, C., Frappart, F., Lubac, B., Bélanger, S., Marieu, V., Blarel, F., Robinet, A., and
728 Guiastrenec-Faugas, L., 2018. Quantification of surface water volume changes in the
729 Mackenzie Delta using satellite multi-mission data. *Hydrol. Earth Syst. Sci.*, 22, 1543-
730 1561, doi: 10.5194/hess-22-1543-2018.

731 Rainboth, W.J., 1996. Fishes of the Cambodian Mekong. FAO Species Identification Field
732 Guide for Fishery Purposes. FAO, Rome, ISBN 92-5-103743-4.

733 Räsänen, T.A., Kummu, M., 2013. Spatiotemporal influences of ENSO on precipitation and
734 flood pulse in the Mekong River Basin. *J. Hydrol.* 476, 154–168.
735 doi:10.1016/j.jhydrol.2012.10.028

736 Rayner, N.A., 2003. Global analyses of sea surface temperature, sea ice, and night marine air
737 temperature since the late nineteenth century. *J. Geophys. Res.* 108.
738 doi:10.1029/2002JD002670

739 Rosenzweig, C., Casassa, G., Karoly, D.J., Imeson, A., Liu, C., Menzel, A., Rawlins, S., Root,
740 T.L., Seguin, B., Tryjanowski, P., 2007. Assessment of observed changes and responses in
741 natural and managed systems. *Climate Change 2007: Impacts, Adaptation and*
742 *Vulnerability. Contribution of Working Group II to the Fourth Assessment Report of the*
743 *Intergovernmental Panel on Climate Change*, Parry, M.L., Canziani, O.F., Palutikof, J.P.,
744 van der Linden, P.J., Hanson, C.E., Eds., Cambridge University Press, Cambridge, UK, 79-
745 131.

746 Sakamoto, T., Van Nguyen, N., Kotera, A., Ohno, H., Ishitsuka, N., Yokozawa, M., 2007.
747 Detecting temporal changes in the extent of annual flooding within the Cambodia and the
748 Vietnamese Mekong Delta from MODIS time-series imagery. *Remote Sens. Environ.* 109,
749 295–313. doi:10.1016/j.rse.2007.01.011

750 Santos da Silva, J., Calmant, S., Seyler, F.,
751 Rotunno Filho, O.C., Cochonneau, G., Mansur, W.J., 2010. Water levels in the Amazon
752 basin derived from the ERS 2 and ENVISAT radar altimetry missions. *Remote Sens.*
753 *Environ.* 114, 2160–2181. doi:10.1016/j.rse.2010.04.020

754 Schindler, D.W., 2009. Lakes as sentinels and integrators for the effects of climate change on
755 watersheds, airsheds, and landscapes. *Limnol. Oceanogr.* 54, 2349–2358.
756 doi:10.4319/lo.2009.54.6_part_2.2349

757 Siev, S., Paringit, E., Yoshimura, C., Hul, S., 2016. Seasonal Changes in the Inundation Area
758 and Water Volume of the Tonle Sap River and Its Floodplain. *Hydrology* 3, 33.
759 doi:10.3390/hydrology3040033

760 Stone, R., 2010. Severe Drought Puts Spotlight on Chinese Dams. *Science* 327, 1311–1311.
761 doi:10.1126/science.327.5971.1311

762 Sverdrup-Jensen, S., 2002. Fisheries in the Lower Mekong Basin: Status and Perspectives.
763 MRC Technical Paper No6, Mekong River Commission, Phnom Penh. 130 pp. ISSN:
764 1683-1489.

765 Tangdamrongsub, N., Ditmar, P.G., Steele-Dunne, S.C., Gunter, B.C., Sutanudjaja, E.H.,
766 2016. Assessing total water storage and identifying flood events over Tonlé Sap basin in
767 Cambodia using GRACE and MODIS satellite observations combined with hydrological
768 models. *Remote Sens. Environ.* 181, 162–173. doi:10.1016/j.rse.2016.03.030

769 UNESCO (2006). Biosphere Reserves - World network, UNESCO - MAB Secretariat, Paris,
770 France. Available at: <http://www.unesco.org/mab/>.

771 Västilä, K., Kummu, M., Sangmanee, C., Chinvano, S., 2010. Modelling climate change
impacts on the flood pulse in the Lower Mekong floodplains. *J. Water Clim. Change* 01,

772 67. doi:10.2166/wcc.2010.008

773 Vu, P-L., Frappart, F., Darrozes, J., Marieu, V., Blarel, F., Ramillien, G., Bonnefond, P., Birol, F.,
774 2018. Multi-Satellite Altimeter Validation along the French Atlantic Coast in the Southern Bay of
775 Biscay from ERS-2 to SARAL. *Remote Sensing* 10(1), 93. doi:10.3390/rs10010093

776 Wang, B., Fan, Z., 1999. Choice of South Asian Summer Monsoon Indices. *Bull. Am.*
777 *Meteorol. Soc.* 80, 629–638. doi:10.1175/1520-0477(1999)080<0629:COSASM>2.0.CO;2

778 Wang, B., Wu, R., Lau, K.-M., 2001. Interannual Variability of the Asian Summer Monsoon:
779 Contrasts between the Indian and the Western North Pacific–East Asian Monsoons*. *J.*
780 *Clim.* 14, 4073–4090. doi:10.1175/1520-0442(2001)014<4073:IVOTAS>2.0.CO;2

781 Williamson, C.E., Saros, J.E., Schindler, D.W., 2009. CLIMATE CHANGE: Sentinels of
782 Change. *Science* 323, 887–888. doi:10.1126/science.1169443

783 Williamson, C.E., Saros, J.E., Vincent, W.F., Smol, J.P., 2009. Lakes and reservoirs as
784 sentinels, integrators, and regulators of climate change. *Limnol. Oceanogr.* 54, 2273–2282.
785 doi:10.4319/lo.2009.54.6_part_2.2273

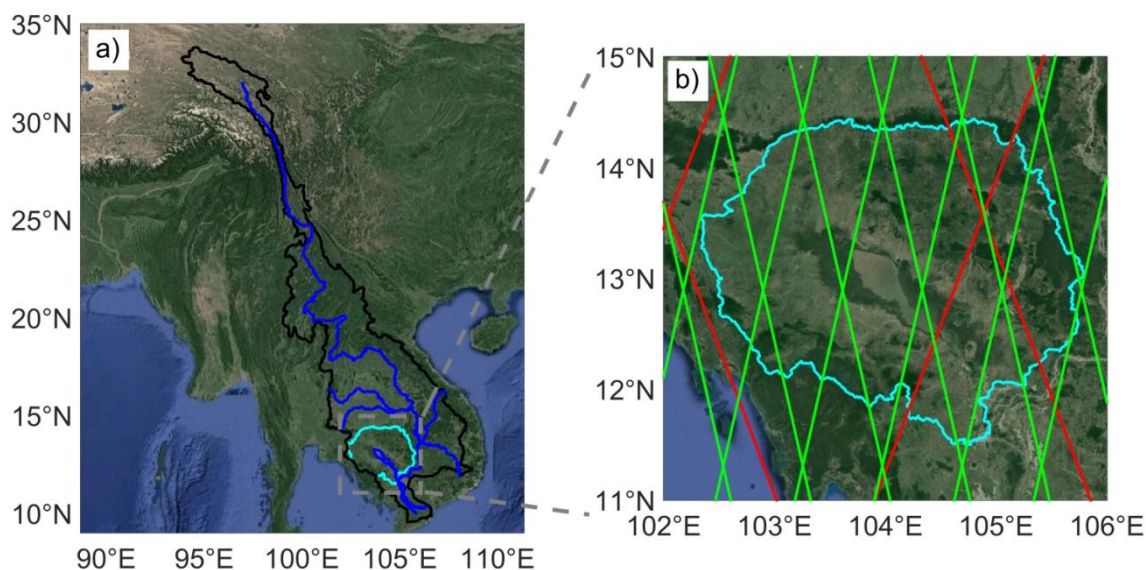
786 WUP-FIN (2003) Modelling Tonle Sap for Environmental Impact Assessment and
787 Management Support, MRCS/WUP-FIN Project. Final Report (Phnom Penh: Mekong
788 River Commission).

789

790

791 Figures:

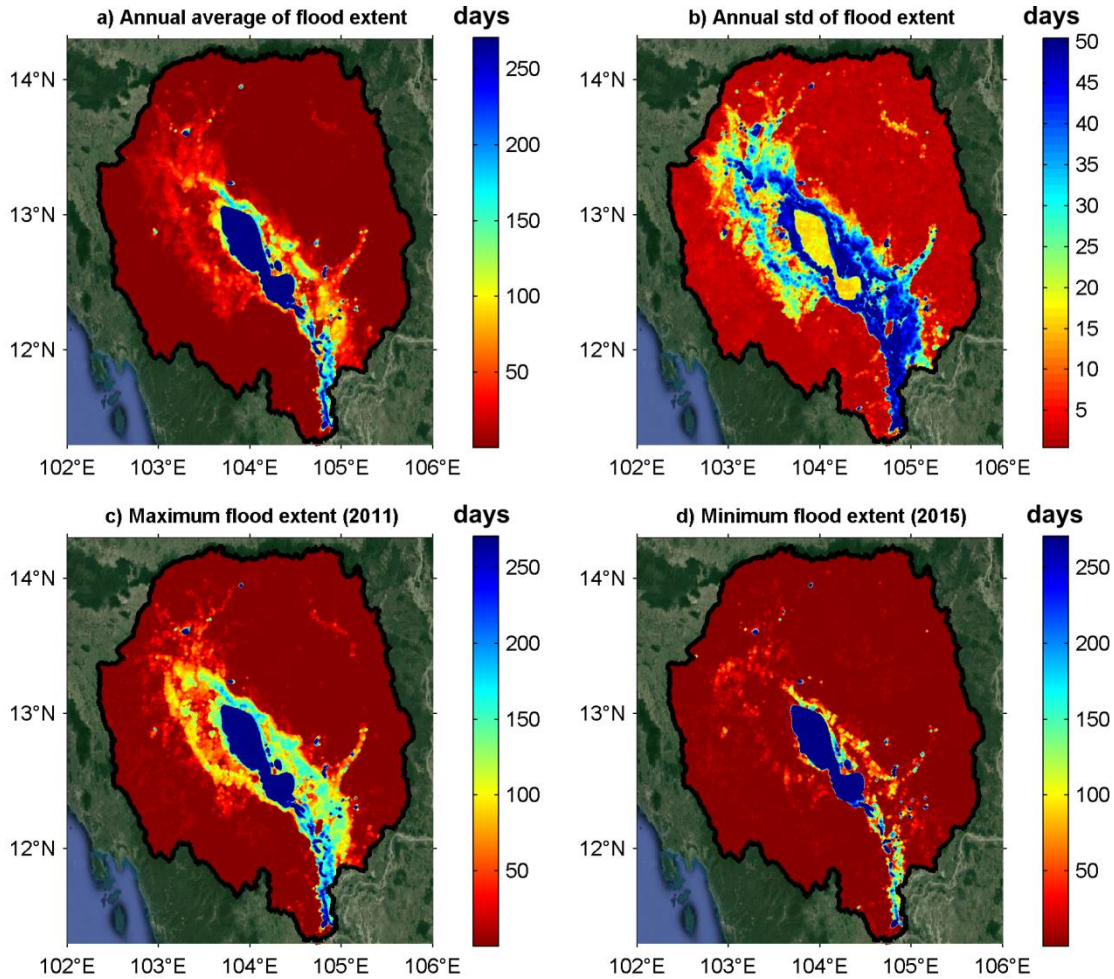
792 Figure 1: a) The Tonle Sap watershed (cyan) is located in the Mekong River Basin (black), the
793 Mekong River and its major tributaries appear in blue; b) 10-day (Jason-1, 2 and 3 in red) and 35-day
794 (ERS-2, ENVISAT and SARAL in green) repeat period tracks over the Tonle Sap Lake watershed.
795 Mekong River Basin boundary and drainage network come from the Major River Basins of the World
796 from the Global Runoff Data Centre - Federal Institute of Hydrology (BfG) available at
797 http://www.bafg.de/GRDC/EN/02_srvcs/22_gslrs/221_MRB/riverbasins_node.html. Tonle Sap
798 boundaries were provided by Open Development Cambodia
799 (<http://www.opendevdevelopmentcambodia.net/maps/downloads/>). Altimetry tracks were provided by
800 AVISO+ (<https://www.aviso.altimetry.fr/en/data/tools/pass-locator.html>). Background images come
801 from Google Earth.



802

803
804
805
806
807

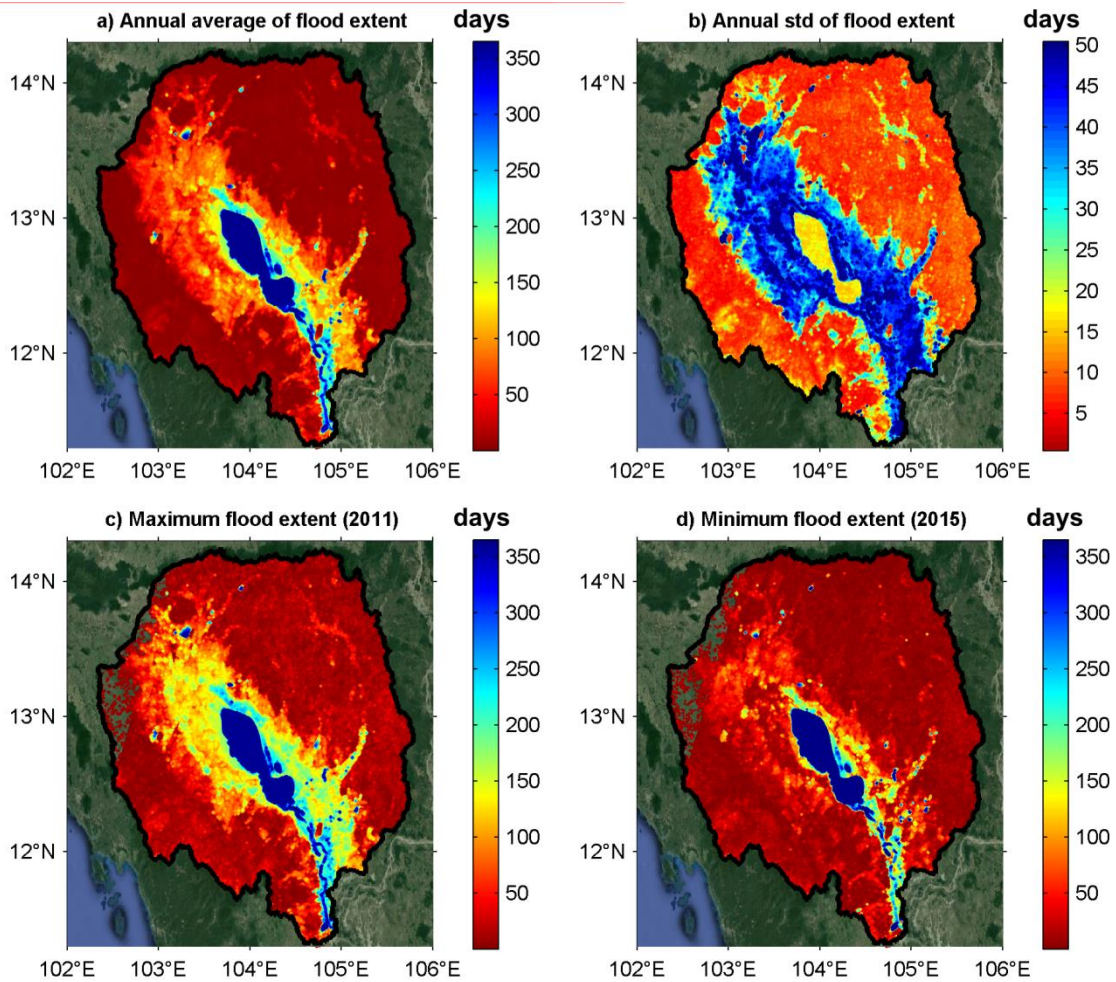
Figure 2: a) Maps of annual flood duration averaged over 2000/2017 time period and b) associated standard deviations expressed in days, using only pixels classified as “inundated”. c) Maps of flood duration in 2011 (year with the maximum flood extent over the whole time period) and d) in 2015 (year with the minimum flood extent), considering only pixels classified as inundated. Background images come from Google Earth.



808

809
810
811
812
813

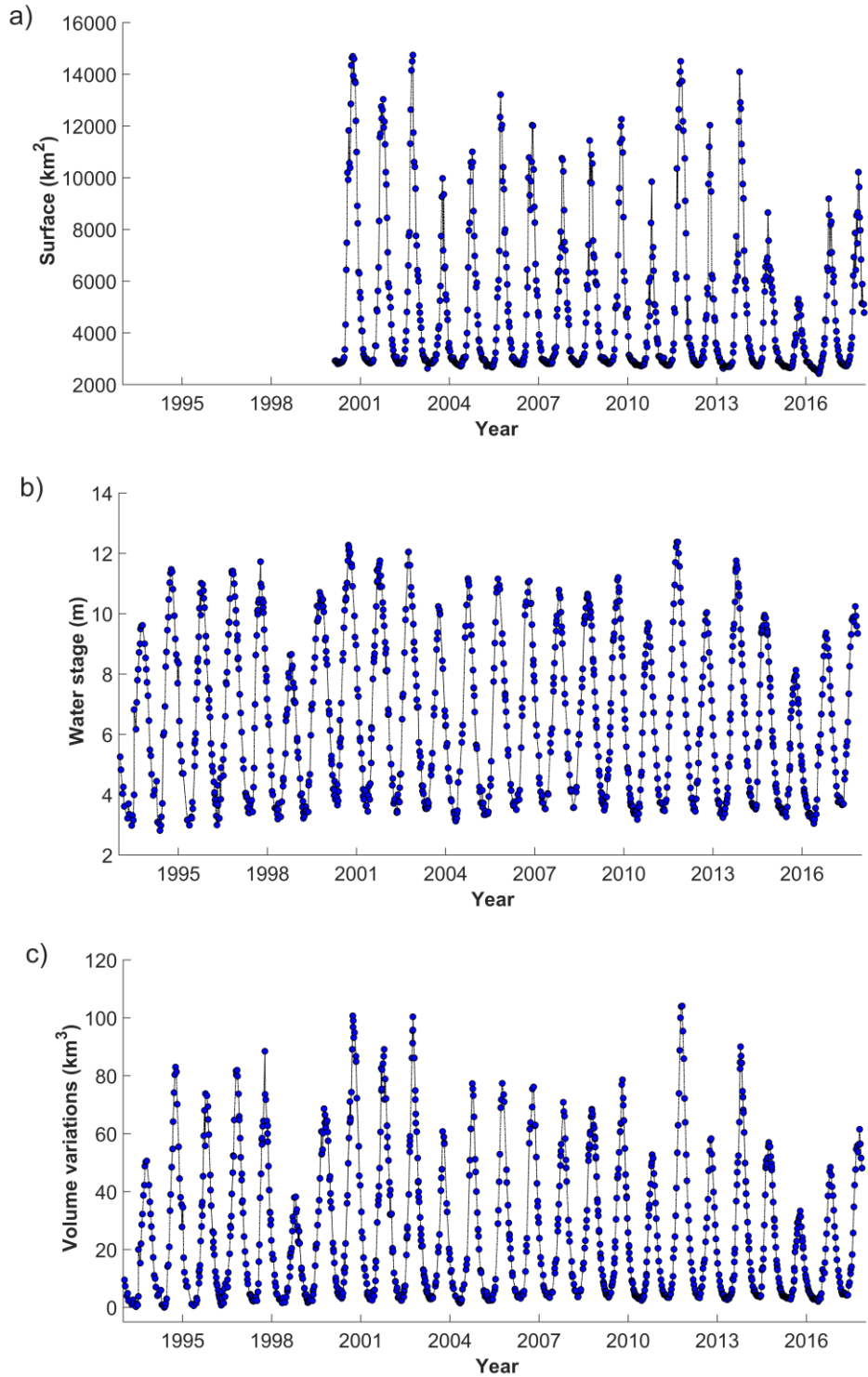
Figure 3: a) Maps of annual flood duration averaged over 2000/2017 time period and b) associated standard deviations expressed in days, using pixels classified as “inundated” and pixels classified as “mixed pixels”. c) Maps of flood duration in 2011 (year with the maximum flood extent) and d) in 2015 (year with the minimum flood extent), considering inundated and mixed pixels. Background images come from Google Earth.



814

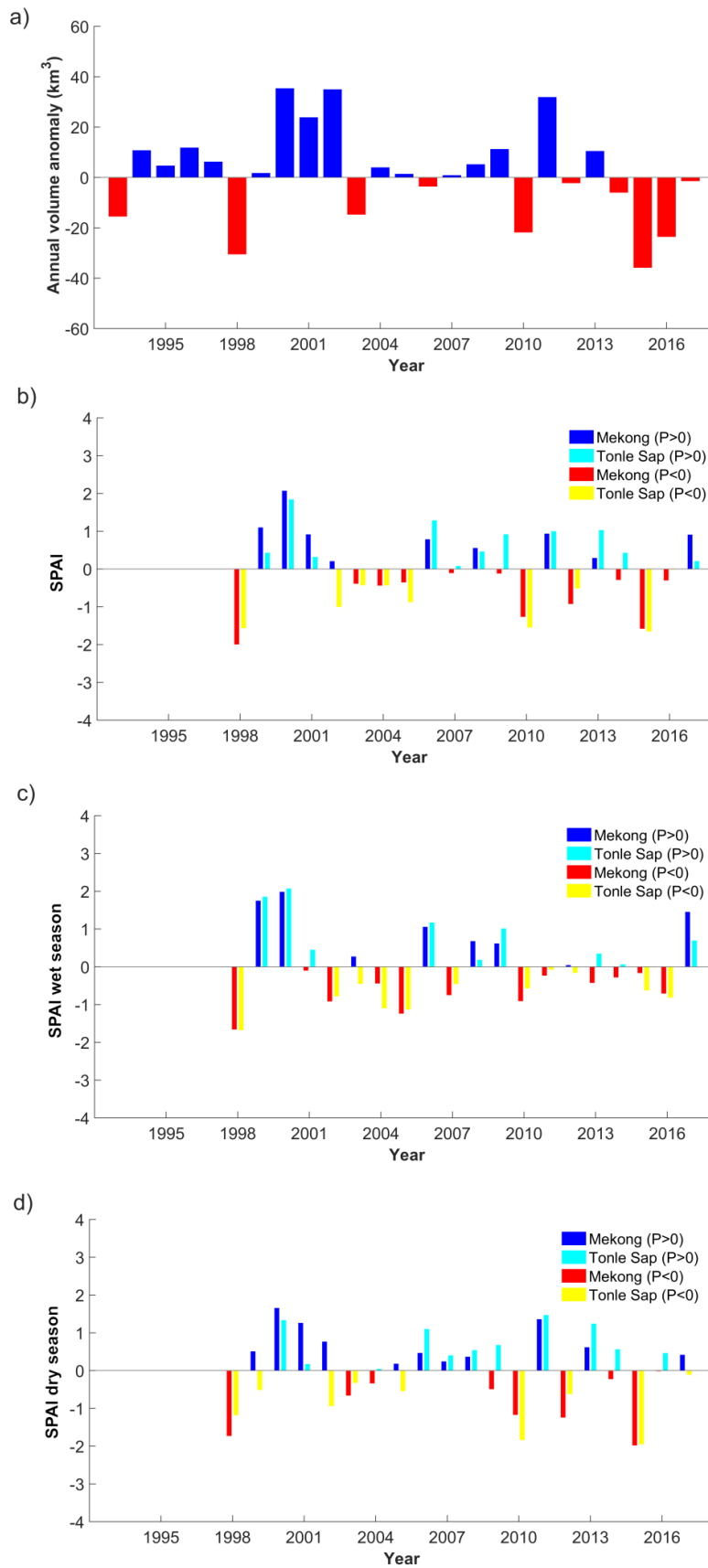
815
816
817
818
819
820

Figure 4: Time series of a) surface water extent (in km^2) in the Tonle Sap basin based on the processing of MODIS images, over 2000-2017, b) altimetry-based water level of the Tonle Sap Lake (in m wrt EGM08 geoid), combining information from Topex/Poseidon (1993-2002), ERS-2 (1995-2003), Jason-1 (2002-2008), ENVISAT (2003-2010), Jason-2 (2008-2016), SARAL (2013-2016) and Jason-3 (since 2016), c) water volume variations of the Tonle Sap lake obtained applying the surface-height relationship over 1993-2017.



821

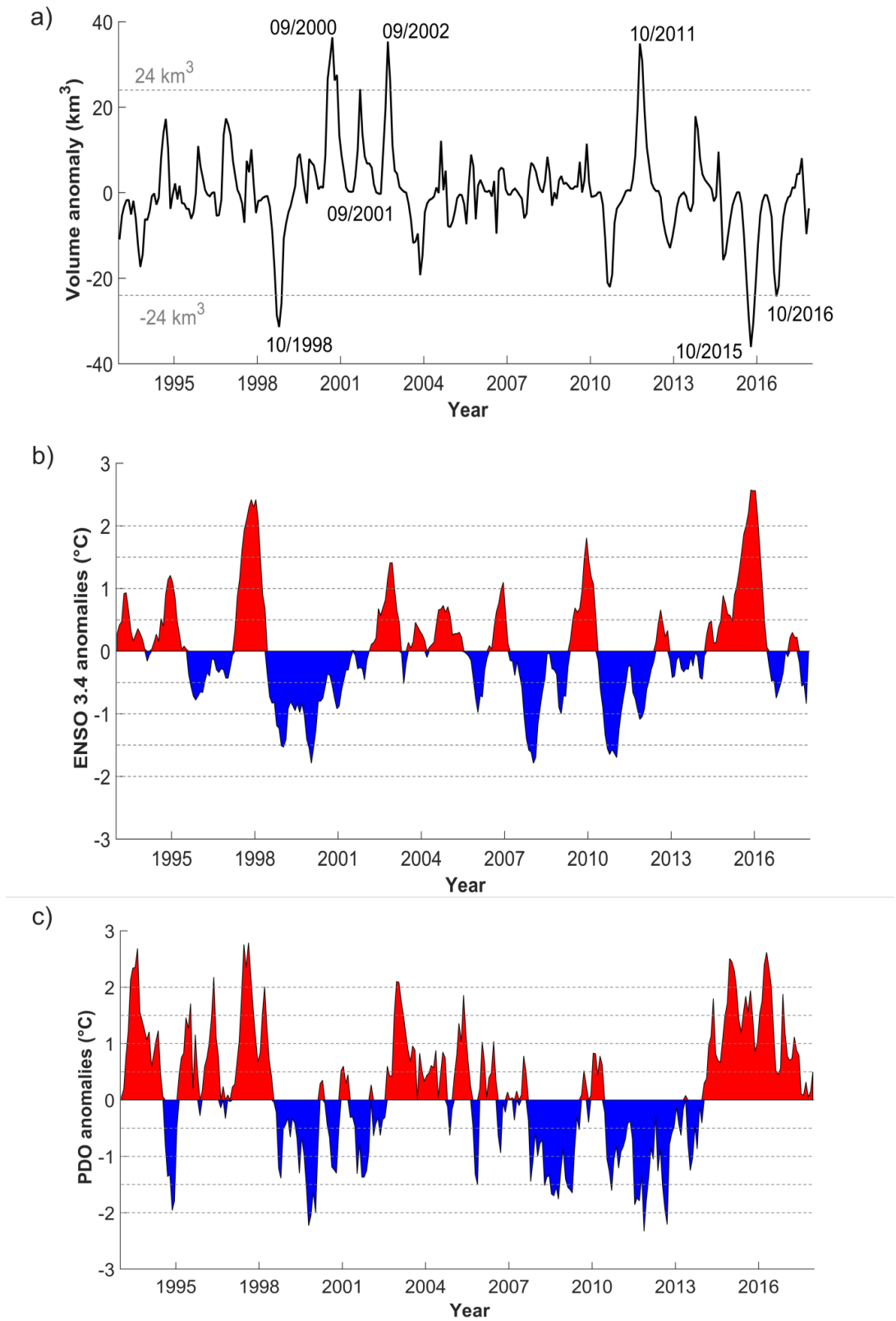
822 Figure 5: a) Interannual variations of annual surface water storage. b) Annual, c) dry and d) wet
823 seasons SPAI in the Mekong Basin and in the Tonle Sap watershed.



824

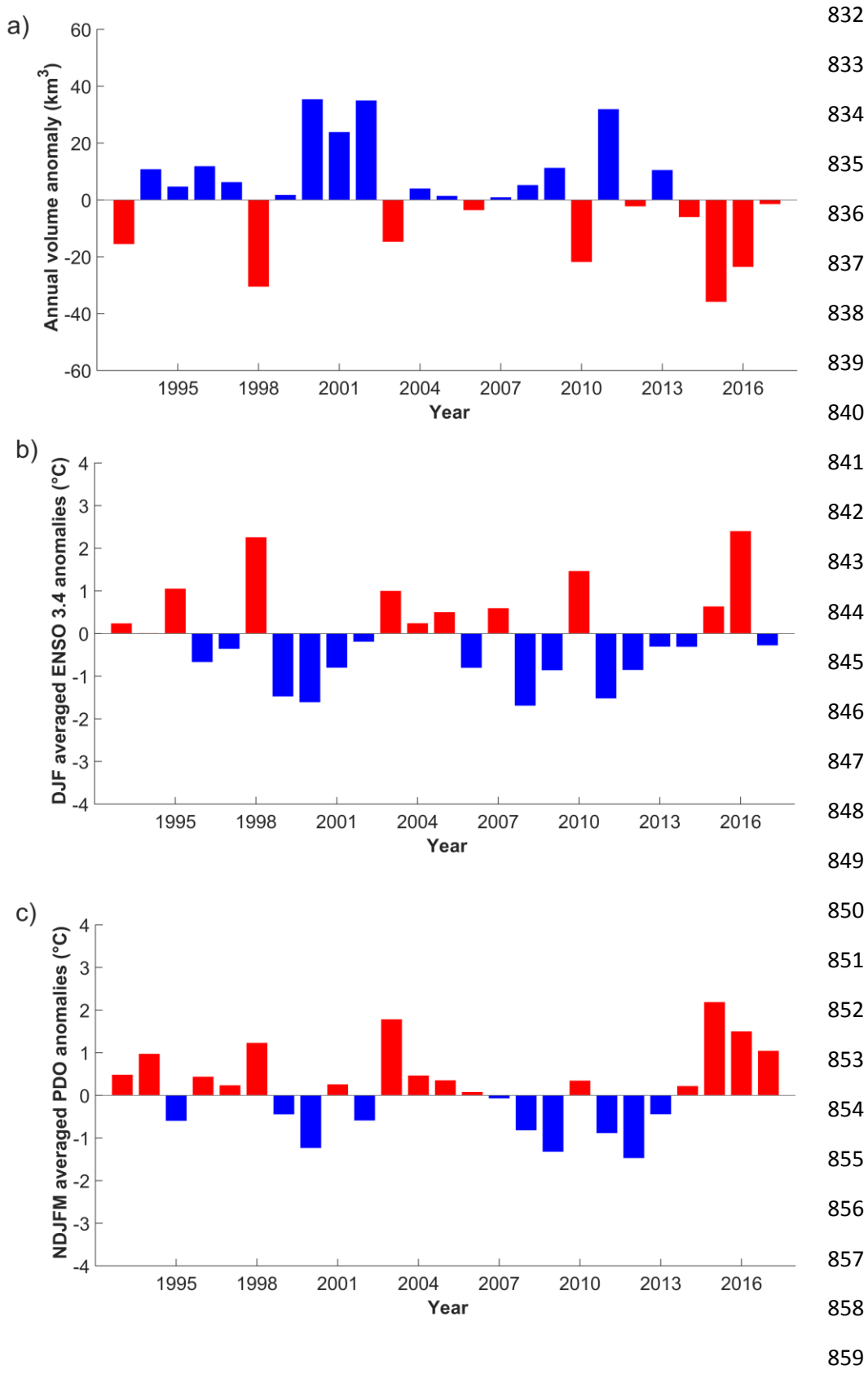
825
826

Figure 6: Interannual variations of monthly a) surface water volume of the Tonle Sap watershed, b) anomalies of ENSO 3.4 and c) PDO indices over 1993-2017.



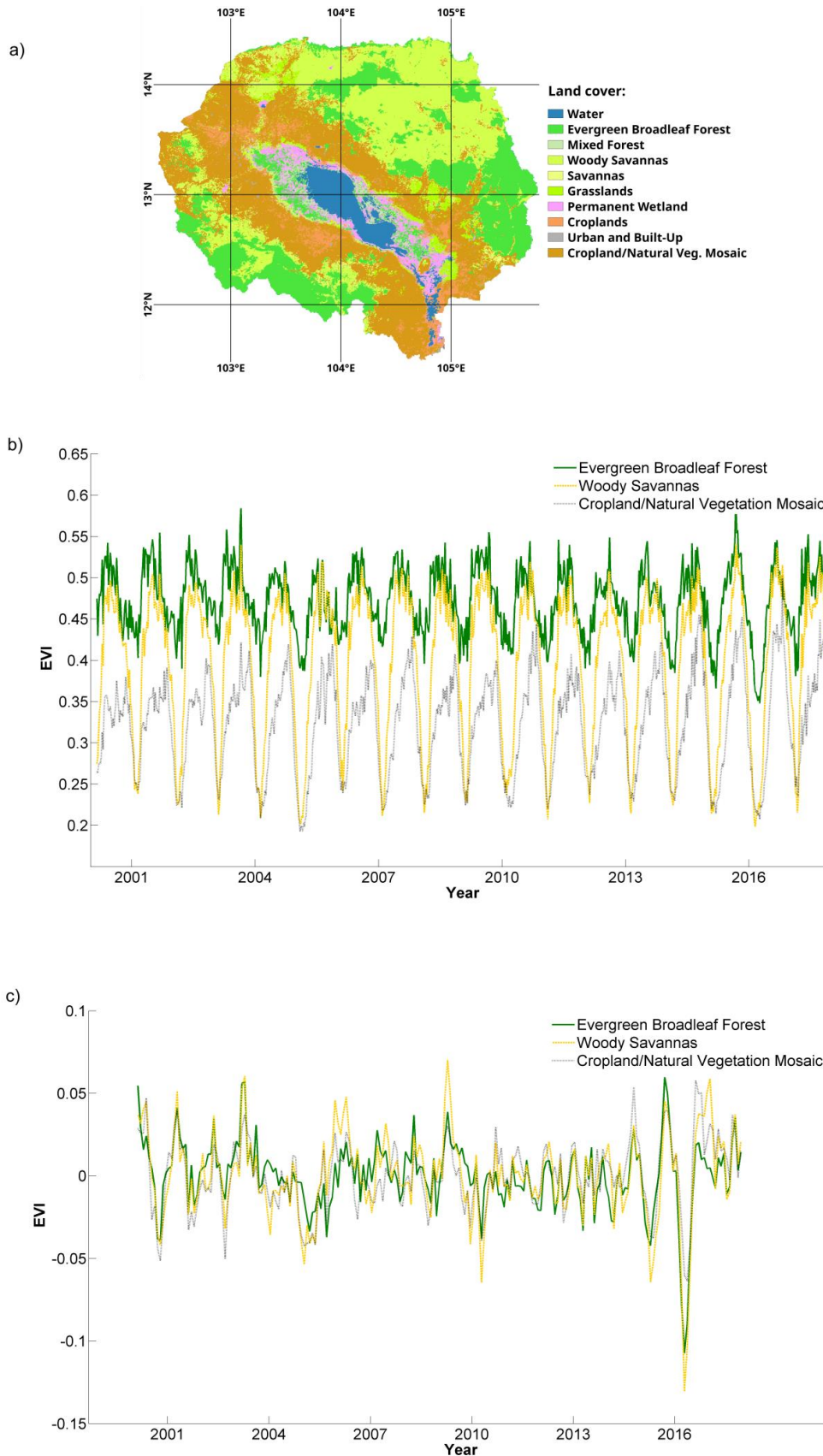
827
828

829 Figure 7: Interannual variations of annual a) surface water storage between 1993 and 2017, b)
 830 anomalies of ENSO 3.4 averaged over December to February (DJF) and c) PDO averaged over
 831 November to March (NDJFM).



860
861
862

Figure 8: a) Land cover map of the Tonle Sap watershed from the 500 m MODIS-based Global Land Cover Climatology, b) time series of EVI and c) EVI interannual anomaly averaged over Evergreen Broadleaf Forest (green), Woody Savannas (orange) and Cropland/Natural Vegetation Mosaic (black).



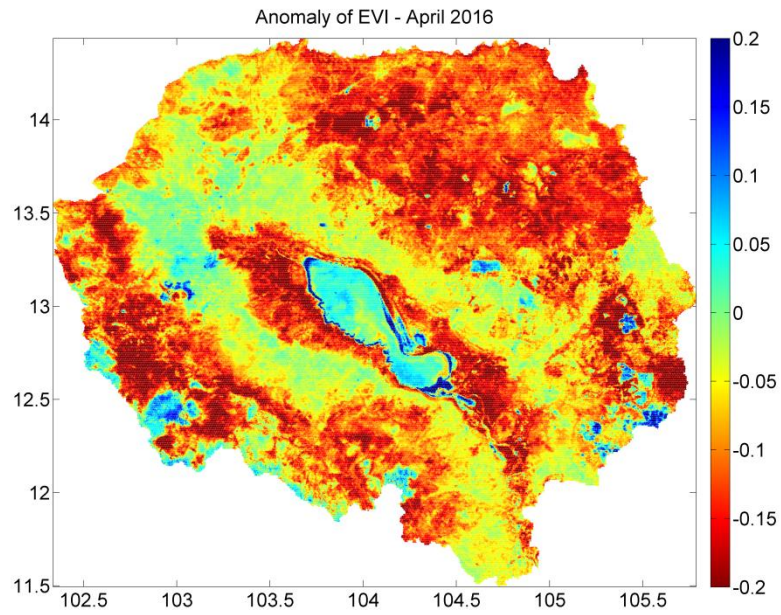
863

864

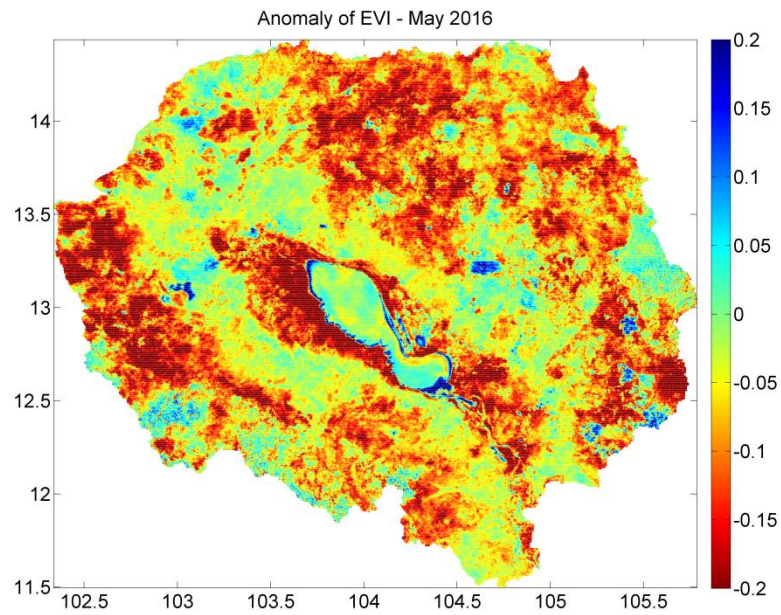
865

Figure 9: Anomaly maps of EVI over the Tonle Sap watershed for a) April and b) May (b) 2016.

a)



b)



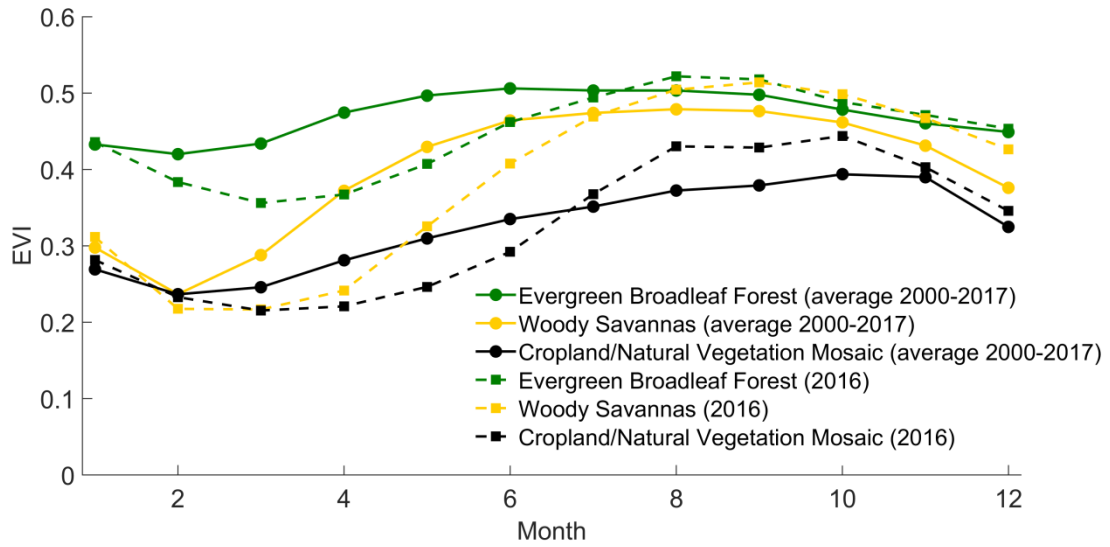
866

867

868

869

870 Figure 10: Monthly variations of EVI averaged over 2000-2017 (continuous line) and EVI for 2016
 871 (dotted line) for the Evergreen Broadleaf Forest (green), Woody Savannas (orange) and
 872 Cropland/Natural Vegetation Mosaic (black).



873